

Preliminary results of using k-Nearest Neighbours Regression to estimate the redshift of radio selected datasets

KIERAN J. LUKEN,^{1,2} RAY P. NORRIS,^{1,2} AND LAURENCE A. F. PARK¹

¹Western Sydney University

Locked Bag 1797

Penrith, NSW 2751, Australia

²CSIRO Astronomy and Space Sciences

Australia Telescope National Facility

PO Box 76, Epping, NSW 1710, Australia

(Received September 6, 2018; Revised October 1, 2018; Accepted October 23, 2018)

Submitted to PASP

ABSTRACT

In the near future, all-sky radio surveys are set to produce catalogues of tens of millions of sources with limited multi-wavelength photometry. Spectroscopic redshifts will only be possible for a small fraction of these new-found sources. In this paper, we provide the first in-depth investigation into the use of k -Nearest Neighbours (kNN) Regression for the estimation of redshift of these sources. We use the Australia Telescope Large Area Survey (ATLAS) radio data, combined with the Spitzer Wide-Area Infrared Extragalactic Survey (SWIRE) infra-red, the Dark Energy Survey (DES) optical and the Australian Dark Energy Survey (OzDES) spectroscopic survey data. We then reduce the depth of photometry to match what is expected from upcoming Evolutionary Map of the Universe (EMU) survey, testing against both data sets. To examine the generalisation of our methods, we test one of the sub-fields of ATLAS against the other. We achieve an outlier rate of $\sim 10\%$ across all tests, showing that the kNN regression algorithm is an acceptable method of estimating redshift, and would perform better given a sample training set with uniform redshift coverage.

Keywords: methods: analytical — methods: statistical — galaxies: distances and redshifts — galaxies: statistics — distance scale

1. INTRODUCTION

Large scale radio surveys are becoming more common, resulting in catalogues of millions of radio sources with limited multi-wavelength data (Norris 2017). Knowledge of their redshift is important to achieve most science goals (Norris et al. 2011). While spectroscopic redshifts remain the gold standard, only a few million spectroscopic redshifts will be available in this decade with the Sloan Digital Sky Survey (SDSS) having measured ~ 3 million over the northern sky (Abolfathi et al. 2018), the Taipan Galaxy Survey expecting to provide 2 million spectroscopic redshifts out to a redshift of $z = 0.4$ (da Cunha et al. 2017), and the Wide Area VISTA

Extra-galactic Survey (WAVES) expecting to measure 2.5 million redshifts across the southern sky out to a redshift of $z = 1.5$ (Driver et al. 2016). Alternatively, redshift can also be measured photometrically, by comparing the magnitudes at different wavelengths to templates (Baum 1962; Butchins 1981; Loh & Spillar 1986). Photometric redshifts - or photo- z 's - measured using template fitting can be highly accurate, estimating redshift to an accuracy of $\sigma_{\Delta z/(1+z_{spec})} \sim 0.015$ (Salvato et al. 2011). However, this requires high quality photometry in at least 15 different filter bands, and up to 31 different bands for the high-accuracy results. Unfortunately, this level of photometry will not be available for large scale sky-surveys. Additionally, photometric template fitting methods tend to fail catastrophically when attempted on AGN, particularly radio-selected AGN (Duncan et al. 2018; Salvato et al. 2018).

Rather than measuring the redshift directly in the form of spectroscopy, or indirectly by fitting templates, it has been shown that photo-z’s can be estimated empirically using the knowledge of previously measured redshifts from similar astronomical objects.

Machine learning has been applied to this problem in the past in the form of neural networks (Tagliaferri et al. 2003; Firth et al. 2003; Collister & Lahav 2004; Cavuoti et al. 2012; Brescia et al. 2013; Cavuoti et al. 2014, 2015; Sadeh et al. 2016; Cavuoti et al. 2017; Pasquet-Itam & Pasquet 2018), random forests (Carliles et al. 2010; Carrasco et al. 2015; Mountrichas et al. 2017), the combination of template fitting methods using Bayesian statistics (Duncan et al. 2018) and the stacking of a Self-Organised Map and a Decision Tree (Zitlau et al. 2016). For the most part, these methods have mainly been concerned with maximising the accuracy of the measured redshift, testing with optically selected galaxy samples, and have been able to achieve a similar accuracy to template fitting methods given a large enough training set. The datasets used have been derived mainly from optical surveys like the SDSS, limiting the number of possible radio-loud AGN, which also create issues for photometric template fitting.

Norris et al. (2018) have addressed the problem of relatively low-quality photometry available from all-sky surveys by comparing the performance of different algorithms when using photometry similar to the upcoming EMU survey (Norris et al. 2011), using radio-selected AGN. This has given a glimpse of the expected accuracies of various techniques when the depth of observations and the coverage of all frequency bands is not complete.

This paper provides a deeper investigation into the effectiveness of the kNN algorithm (Cover & Hart 1967) for estimating redshift. The kNN regression algorithm has previously been applied to photometric redshifts by Polsterer et al. (2013), Kügler et al. (2015) and Cavuoti et al. (2017), however Kügler et al. (2015) used optical spectra from the Sloan Digital Sky Survey (SDSS), and Polsterer et al. (2013) and Cavuoti et al. (2017) used spectroscopic redshifts and optical magnitudes only from the SDSS. k Nearest Neighbours Regression is a regression model, meaning that it uses a training set of objects and their known redshift values to estimate the redshift of new objects. In particular, kNN regression estimates the redshift of each new object as the mean of the redshifts of the k nearest neighbours from the training set. To perform this task, we must define a feature space (so that we can represent each object as a vector), a metric (to provide the distance between object vectors), and the value of the constant k . The feature space dimensions are chosen as the set of variables that

are thought to be predictive of the regression response. Each object is represented as a vector in this space using their measurements of the feature space variables (e.g. in our case each object vectors contain a set of photometry at different wavelengths from a given object in the training set). It is common to find Euclidean distance being used as the kNN metric, and the number of neighbours k typically set within the range of 2 and 20.

Given that the speed of the kNN algorithm does not scale well with the number of dimensions or number of sources, this algorithm can be modified to use a k-d tree to find the k most similar sources (Polsterer et al. 2013). Alternatively, the problem can be parallelised and run on a GPU. This paper has implemented the kNN regression algorithm using the publicly available TensorFlow¹ on GPU (Abadi et al. 2015), which provides a 3-5 times speed improvement over the equivalent CPU version.

Our initial investigation was to determine the suitability of kNN for the problem. We then tested how well the kNN algorithm generalises by testing one sub-field against the other. We next modified our dataset to match the depth expected from the EMU survey, and corresponding sky surveys from other astronomical regimes. For all of these tests, we compared the use of Euclidean distance and Manhattan Taxicab distance.

2. THE DATA

The dataset used in this paper is primarily based on the ATLAS Data Release 3 (Norris et al. 2006; Franzen et al. 2015), with cross-identifications to other wavelengths provided by Swan et al. (in preparation). Other catalogues used include the SWIRE Infra-red dataset (Lonsdale et al. 2003), the DES Optical dataset (Abbott et al. 2018) and the OzDES spectroscopic redshift dataset (Yuan et al. 2015; Childress et al. 2017).

2.1. ATLAS

The ATLAS DR3 dataset (Franzen et al. 2015) forms the basis for our total catalogue, providing 1.4 GHz radio flux densities on 4780 sources measured using the Australia Telescope Compact Array (ATCA). The ATLAS dataset covers the European Large Area ISO Survey–South 1 (ELAIS-S1) and extended Chandra Deep Field South (eCDFs) fields, down to a r.m.s noise level of $\sim 15\mu\text{Jy}$.

2.2. SWIRE

The SWIRE dataset provides infra-red flux densities at 3.6, 4.5, 5.8 and 8.0 μm , measured using the Spitzer Space Telescope (SST) (Lonsdale et al. 2003), reaching a

¹ <https://www.tensorflow.org/>

5σ sensitivity of 5, 9, 43 and 40 $\mu\text{Jy}/\text{beam}$ respectively. SWIRE identifications were found for 4328 radio sources at 3.6 μm , providing at least a 3.6 μm flux for $\sim 91\%$ of radio sources. All ATLAS sources were initially cross-matched with SWIRE sources, and then the SWIRE sources were cross-matched to the DES sources.

2.3. DES

The DES dataset provides g , r , i and z optical magnitudes (to a depth of $g = 24.33$, $r = 24.08$, $i = 23.44$ and $z = 22.69$), measured using the Dark Energy Camera mounted on the 4-m Blanco telescope at Cerro Tololo Inter-American Observatory in Chile. (Abbott et al. 2018). The DES dataset provides optical counterparts for 3102 of our radio sources at g band, covering $\sim 65\%$ of sources.

2.4. OzDES

The OzDES dataset provides the spectroscopic redshifts required to create any empirical model (Yuan et al. 2015; Childress et al. 2017). The spectroscopic redshift master list compiled as the OzDES dataset by Childress et al. (2017) provides spectroscopic redshifts for 2012 radio sources, covering $\sim 42\%$ of sources.

2.5. Test Sample

The kNN algorithm works best if the reference data set is shaped such that the feature space is populated homogeneously, i.e. avoiding strong concentrations in a certain region, or sparsely populated regions. In the tests described here, we made no correction for any excess sources in any of the given training samples. Instead, we calculated optical and infrared colours as $c_i = \text{mag}_i - \text{mag}_{i+1}$. This transformation improves the distribution of the photometric data over the parameter space for each band (Norris et al. 2018) and also replaces flux, which is brightness- and redshift-dependent, by colour that depends only on the SED (Polsterer et al. 2013). We completed this transformation on both the optical magnitudes, and log-transformed infra-red fluxes. Note that this operation reduces the effective number of dimensions of the feature space by 2.

We compiled a a full-sensitivity ‘‘DEEP’’ sample containing those sources that have photometry at 1.4 GHz, infra-red 3.6, 4.5, 5.8 and 8.0 μm , optical g , r , i and z bands, and a spectroscopic redshift. This provides us with 1408 sources with complete photometry and spectroscopy for our tests.

We then selected a ‘‘WIDE’’ sample to match the depth of photometry expected from the EMU survey (Norris et al. 2011), which will use the SkyMapper survey which has r and i limits of ≈ 22 (Wolf et al. 2018)

and the AllWISE Infrared Survey (Cutri & et al. 2013) of 3.6 $\mu\text{m} > 26 \mu\text{Jy}$ and 4.5 $\mu\text{m} > 56 \mu\text{Jy}$. We removed the 5.8 and 8.0 μm data from our sample, and rejected any sources which were undetected at any band at the above limits. The resulting WIDE sample had 760 sources.

As discussed in Section 2.1, the ATLAS catalogue covers two fields. The ELAIS-S1 field, which makes up 553 of the 1408 sources in the DEEP data set and 281 of the 760 sources in the WIDE data set, and the eCDFs field, which makes up 855 of the 1408 sources in the DEEP dataset and 479 of the 760 sources in the WIDE data set.

3. EXPERIMENTS

In these experiments, we use the kNN regression algorithm to estimate redshifts, using the following steps:

1. Compute a distance matrix between all test sources and training sources.
2. Sort the distance matrix by the distance calculated in step 1, identifying the k closest training sources in feature space to the test sources
3. Take the mean redshift of the known sources identified from step 2, and assign it to the test source.

To apply this method, we split our data into a training and test set. Depending on the test being run, the training set was either 70% of the data set in the case of the full dataset tests (Tests 1-4 in Table 1), or the entire sub field in the case of the sub-field tests (Tests 5-12 in Table 1). The remaining 30% or sub-field was set aside as the test set.

To avoid under- or over-fitting the data, 10-fold cross validation was used with our training sets - excluding our test sets, minimising the number of incorrect estimates. In all tests, the value of k that minimised the outlier rate varied, and is listed in Table 2.

We computed 95% confidence intervals for each redshift prediction using bootstrapping with 1000 iterations. Bootstrapping is a sampling method that allows us to estimate the variance of sample estimates under the assumption that the population from which the sample is taken is approximately many replications of the sample. The estimated intervals provide the range in which the true redshift is likely to occur, while also providing an indication of the uncertainty of the prediction. These confidence intervals are displayed in the form of error bars in our figures in Section 4.

In our investigation of the accuracy of kNN, we examined the effect of varying the following experimental parameters:

- **Distance Metric:** We evaluated both the Euclidean distance metric:

$$d(\vec{p}, \vec{q}) = \sqrt{\sum_{i=1}^n (q_i - p_i)^2} \quad (1)$$

and the Manhattan Taxicab distance metric:

$$d(\vec{p}, \vec{q}) = \|\vec{p} - \vec{q}\| = \sum_{i=1}^n |p_i - q_i| \quad (2)$$

Where p and q are vectors containing the features of two sources.

- **Depth of Photometry:** We used both the full-sensitivity DEEP sample and the reduced-sensitivity WIDE sample.
- **Generalisation:** We randomly selected training and test sets from both ATLAS sub-fields as one test, and used one ATLAS sub-field as the training set and the other as the test set and reverse as additional tests.

As these variations are not independent, each needed to be completed in combination with all others, resulting in the 12 experiments listed in Table 1.

4. RESULTS

We present the results of the experiments in Table 2 and Figures 1 to 3.

In Table 2 and Figures 1 to 3, we calculate the outlier rate η as:

$$\eta = \frac{\text{count}(|\Delta z| > 0.15 \times (1 + z_{spec}))}{\text{Number Of Sources}} \times 100 \quad (3)$$

where $\Delta z = z_{spec} - z_{photo}$ and the normalised median absolute deviation σ_{NMAD} as:

$$\sigma_{NMAD} = 1.4826 \times \text{median}(|X_i - \text{median}(X)|) \quad (4)$$

where X is a vector of residuals

In Figures 1, 2 and 3, the top panels show the distribution of z_{spec} vs z_{photo} , and the lower panels show the normalised residuals vs the z_{spec} , where the normalised residuals are calculated by:

$$\frac{\Delta z}{z_{spec} + 1}$$

For every source plotted on the top panels, we have provided error bars representing the 95% confidence interval of each redshift, calculated using the bootstrap method. On each of the plots, we display multiple statistics:

- N - The number of sources in the test sample
- σ - Standard deviation of the residual error, calculated typically
- NMAD - Standard deviation of the residual error, calculated using the normalised absolute deviation (Equation 4)
- η - Outlier rate, calculated using Equation 3

These results have all been summarised in Table 2.

4.1. Distance Metric

Across all of our experiments, we have found negligible difference between using the Manhattan Taxicab distance metric and the Euclidean Distance metric. This indicates that there were few significant outliers when finding the k nearest neighbours, as the Manhattan Taxicab distance will minimise the effect of outliers. In Tests 3 vs 4, 7 vs 8, and 11 vs 12, we find that Euclidean Distance provides a slightly lower outlier rate. In Test 5 vs 6 and 9 vs 10, Manhattan Taxicab distance provides the better option with Test 1 vs 2 being equal. In no case however, does one distance metric have a difference in outlier rate greater than 1.78%.

4.2. Depth of Field

In all cases, we find that the outlier rate is higher in the WIDE dataset when compared with the DEEP dataset, as shown by the right-hand pair of panels in Figures 1 to 3. For the kNN regression algorithm, this is expected in current catalogues. In the process of modifying the DEEP dataset to become the WIDE dataset, all sources that we removed are at the fainter end of the dataset, which are typically the high redshift sources. This leaves the WIDE dataset with a more heavily positively skewed distribution of z_{spec} , with the majority of sources being below $z = 0.5$. For the sources at high redshifts, the kNN algorithm tends to fail because of the paucity of high-redshift sources, forcing low-redshift sources into the group of nearest neighbours.

A better test would use a larger data set, with a larger population of high-redshift sources, but such a dataset is not yet available.

4.3. Generalisation

While the best-case DEEP experiments using a random sample as the training set attain the best results, experiments that train on one ATLAS field, and test on a different ATLAS field, are not much worse. We can attribute the better results in the former case to a more uniform and statistically consistent training sample. This indicates that, with a more consistent training

Table 1. Details of experiments completed, including the experiment number, training and test set sizes, the distance metric used, the dataset used and where the training sample came from.

Experiment Number	Size of Training Set	Size of Test Set	Distance Metric	Data set Used	Training Sample
1	986	422	Manhattan	DEEP	Random
2	986	422	Euclidean	DEEP	Random
3	532	228	Manhattan	WIDE	Random
4	532	228	Euclidean	WIDE	Random
5	553	855	Manhattan	DEEP	ELAIS-S1
6	553	855	Euclidean	DEEP	ELAIS-S1
7	281	479	Manhattan	WIDE	ELAIS-S1
8	281	479	Euclidean	WIDE	ELAIS-S1
9	855	553	Manhattan	DEEP	eCDFS
10	855	553	Euclidean	DEEP	eCDFS
11	479	281	Manhattan	WIDE	eCDFS
12	479	281	Euclidean	WIDE	eCDFS

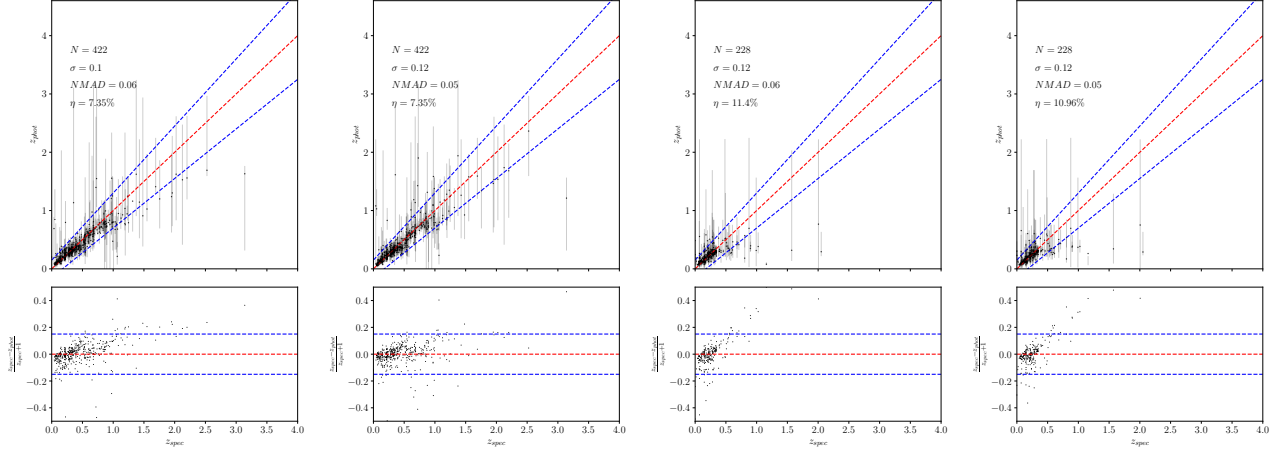


Figure 1. Summary of the results from Tests 1-4, from left to right. All results displayed here have been trained on sources randomly sampled from the entire ATLAS data set. The top panels show the distribution of z_{spec} vs z_{photo} , and the lower panels show the normalised residuals vs the z_{spec} . The dashed red line represents $z_{spec} = z_{photo}$, and the dashed blue lines represent the outlier boundary, calculated using Equation 3.

Table 2. Summary of the results from all tests. We include the experiment number, the test size, standard deviation calculated typically and by normalised absolute deviation and outlier rate.

Experiment Number	Test Size	Best k	Standard Deviation	NMAD	Outlier Rate
1	422	3	0.1	0.06	7.35%
2	422	14	0.12	0.05	7.35%
3	228	3	0.12	0.06	11.40%
4	228	2	0.12	0.05	10.96%
5	855	13	0.13	0.05	11.11%
6	855	9	0.13	0.05	11.46%
7	479	3	0.12	0.06	13.15%
8	479	4	0.12	0.06	12.11%
9	553	4	0.12	0.06	10.31%
10	553	3	0.12	0.06	9.04%
11	281	2	0.13	0.06	13.88%
12	281	2	0.12	0.06	12.10%

sample, the kNN regression algorithm should perform well across different sections of sky.

5. IMPLICATIONS FOR LARGE-SCALE RADIO SURVEYS

Table 2 shows that redshifts can be measured to an accuracy of about 6% (NMAD) to 12% (standard deviation), with an outlier rate of about 11%, and this result remains true for all sources for which photometry is available, independently of the depth of the photometry.

If we assume that the DEEP sample has the same radio sensitivity as EMU, and that the WIDE sample has the same optical/infra-red photometric depth as that available for EMU sources, then the relative sizes of the DEEP and WIDE samples implies that $\sim 45\%$ of EMU sources will have the required photometry for redshift measurement.

We can therefore conclude, based on these tests, that about 40% of EMU sources will have redshifts available, or a total of about 28 million radio sources.

We plan to extend this work by investigating the effect of (a) using the non-detection information, (b) using a more sophisticated metric that allows missing values

and measurement bounds, (c) carefully modelling the sensitivity limits of the available photometric surveys, (d) incorporating other data types (such as radio and X-ray), (e) quantising redshift to provide a classification problem rather than a regression problem, (f) obtaining more high-redshift training data from deep surveys in small fields. Future work will continue in this direction.

6. CONCLUSION

The main result from these preliminary experiments is that, using the kNN algorithm, we can make good estimates of redshifts in large radio surveys given the photometry that is likely to be available, although further work is expected to improve results further. Around 90% of EMU sources with optical/infra-red photometry will have a reliable estimated redshift, resulting in redshifts for $\sim 40\%$ of EMU sources. However, we expect that future work will result in an even higher fraction of sources with useful redshifts.

We found no obvious difference in the results provided by Manhattan Taxicab distance and Euclidean Distance. However, greater benefits may be obtained from self-learned distance metrics that can weight features based on their relevance, and can deal with missing values.

We found that the DEEP dataset reported better results than the WIDE dataset, probably because the WIDE survey contains mainly low-redshift sources with the few high-redshift sources having to be estimated from low-redshift sources. Further work will characterise what fraction of sources have the required photometry at higher redshifts.

We found that there was no obvious difference in success rate if the algorithm used training and test sets from spatially separate fields in the sky. Experiments 7-8 and 11-12 (different field training sets on the WIDE dataset) suggest that we can overcome the lack of high redshift sources in training sets by drawing training sets from small, deep fields and applying them to targets covering the entire sky.

Finally, this paper has demonstrated that with sufficient redshift coverage in the training set, the kNN algorithm provides acceptable error rates when estimating the redshift of radio galaxies.

ACKNOWLEDGEMENTS

We thank Stefano Cavuoti and his colleagues for use of the code to plot our results.

REFERENCES

- Abadi, M., Agarwal, A., Barham, P., et al. 2015, TensorFlow: Large-Scale Machine Learning on Heterogeneous Systems, , software available from tensorflow.org. <https://www.tensorflow.org/>
- Abbott, T. M. C., Abdalla, F. B., Allam, S., et al. 2018, ArXiv e-prints, arXiv:1801.03181

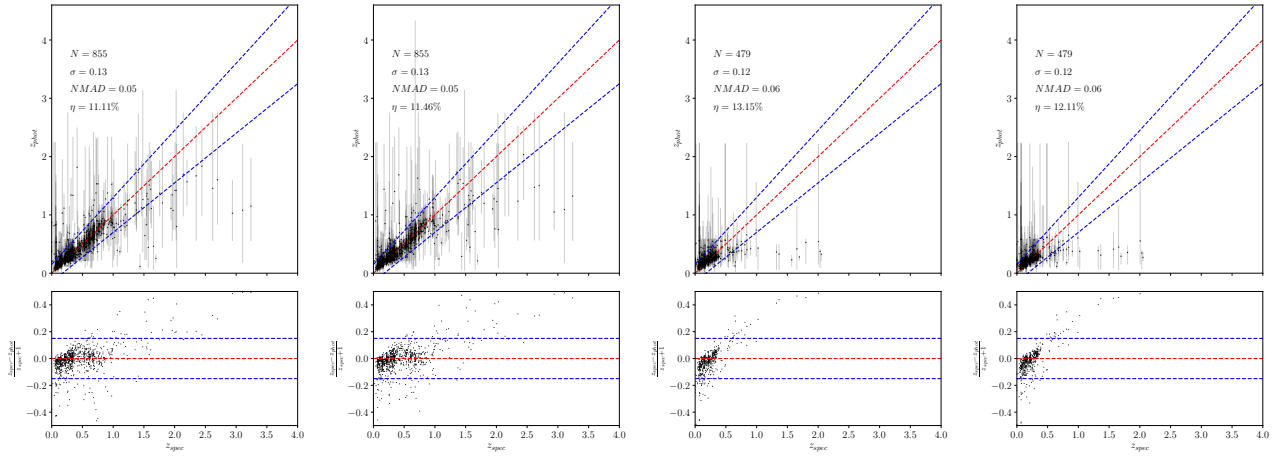


Figure 2. Summary of the results from Tests 5-8, from left to right. All results displayed here have been trained on sources found exclusively in the ELAIS-S1 field. Other details as in Figure 1.

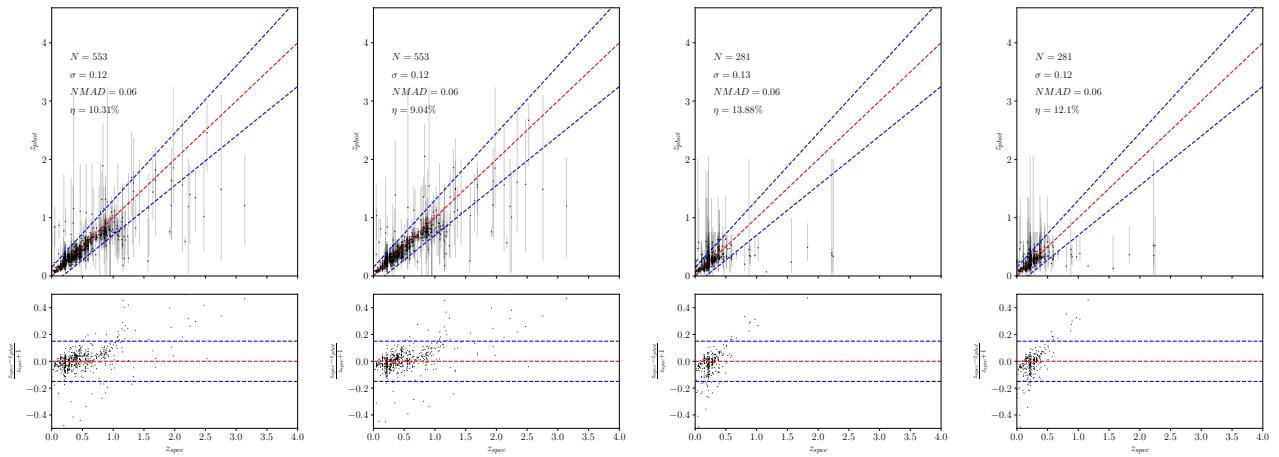


Figure 3. Summary of the results from Tests 9-12, from left to right. All results displayed here have been trained on sources found exclusively in the eCDFs field. Other details as in Figure 1.

- Abolfathi, B., Aguado, D. S., Aguilar, G., et al. 2018, *The Astrophysical Journal Supplement Series*, 235, 42
- Baum, W. A. 1962, in *IAU Symposium*, Vol. 15, *Problems of Extra-Galactic Research*, ed. G. C. McVittie, 390
- Brescia, M., Cavuoti, S., D’Abrusco, R., Longo, G., & Mercurio, A. 2013, *ApJ*, 772, 140
- Butchins, S. A. 1981, *A&A*, 97, 407
- Carliles, S., Budavári, T., Heinis, S., Priebe, C., & Szalay, A. S. 2010, *ApJ*, 712, 511
- Carrasco, D., Barrientos, L. F., Pichara, K., et al. 2015, *A&A*, 584, A44
- Cavuoti, S., Amaro, V., Brescia, M., et al. 2017, *MNRAS*, 465, 1959
- Cavuoti, S., Brescia, M., De Stefano, V., & Longo, G. 2015, *Experimental Astronomy*, 39, 45
- Cavuoti, S., Brescia, M., & Longo, G. 2014, in *IAU Symposium*, Vol. 306, *Statistical Challenges in 21st Century Cosmology*, ed. A. Heavens, J.-L. Starck, & A. Krone-Martins, 307–309
- Cavuoti, S., Brescia, M., Longo, G., & Mercurio, A. 2012, *A&A*, 546, A13
- Childress, M. J., Lidman, C., Davis, T. M., et al. 2017, *MNRAS*, 472, 273
- Collister, A. A., & Lahav, O. 2004, *PASP*, 116, 345
- Cover, T., & Hart, P. 1967, *IEEE Transactions on Information Theory*, 13, 21
- Cutri, R. M., & et al. 2013, *VizieR Online Data Catalog*, 2328
- da Cunha, E., Hopkins, A. M., Colless, M., et al. 2017, *Publications of the Astronomical Society of Australia*, 34, e047
- Driver, S. P., Davies, L. J., Meyer, M., et al. 2016, *The Universe of Digital Sky Surveys*, 42, 205
- Duncan, K. J., Brown, M. J. I., Williams, W. L., et al. 2018, *MNRAS*, 473, 2655
- Firth, A. E., Lahav, O., & Somerville, R. S. 2003, *MNRAS*, 339, 1195
- Franzen, T. M. O., Banfield, J. K., Hales, C. A., et al. 2015, *MNRAS*, 453, 4020
- Kügler, S. D., Polsterer, K., & Hoecker, M. 2015, *A&A*, 576, A132
- Loh, E. D., & Spillar, E. J. 1986, *ApJ*, 303, 154
- Lonsdale, C. J., Smith, H. E., Rowan-Robinson, M., et al. 2003, *PASP*, 115, 897
- Mountrichas, G., Corral, A., Masoura, V. A., et al. 2017, *Astronomy and Astrophysics*, 608, A39
- Norris, R. P. 2017, *Nature Astronomy*, 1, 671
- Norris, R. P., Afonso, J., Appleton, P. N., et al. 2006, *AJ*, 132, 2409
- Norris, R. P., Hopkins, A. M., Afonso, J., et al. 2011, *PASA*, 28, 215
- Norris, R. P., Salvato, M., Longo, G., et al. 2018, *PASP*, submitted
- Pasquet-Itam, J., & Pasquet, J. 2018, *A&A*, 611, A97
- Polsterer, K. L., Zinn, P.-C., & Gieseke, F. 2013, *MNRAS*, 428, 226
- Sadeh, I., Abdalla, F. B., & Lahav, O. 2016, *PASP*, 128, 104502
- Salvato, M., Ilbert, O., & Hoyle, B. 2018, *Nature Astronomy*, arXiv:1805.12574
- Salvato, M., Ilbert, O., Hasinger, G., et al. 2011, *ApJ*, 742, 61
- Tagliaferri, R., Longo, G., Andreon, S., et al. 2003, *Lecture Notes in Computer Science*, 2859, 226
- Wolf, C., Onken, C. A., Luvaul, L. C., et al. 2018, *PASA*, 35, e010
- Yuan, F., Lidman, C., Davis, T. M., et al. 2015, *MNRAS*, 452, 3047
- Zitlau, R., Hoyle, B., Paech, K., et al. 2016, *MNRAS*, 460, 3152